Results in Physics 74 (2025) 108288

Contents lists available at ScienceDirect

Results in Physics

journal homepage: www.elsevier.com/locate/rinp

Strain-tunable electronic, optical and thermoelectric properties of two-dimensional Janus SbXI (X=S, Se, Te) monolayers: A first-principles study

Fredy Mamani Gonzalo [a,*], Victor José Ramirez Rivera [a], Julio R. Sambrano [c], Maurício Jeomar Piotrowski [b], Efracio Mamani Flores [a,*]

[a] Department of Physics, Jorge Basadre Grohmann National University, Tacna, Peru
[b] Department of Physics, Federal University of Pelotas, Pelotas, Rio Grande do Sul, Brazil
[c] Modeling and Molecular Simulation Group, São Paulo State University, Bauru, São, Paulo 17033-360, Brazil

ARTICLE INFO

Keywords:
Absorption coefficient
BTT
DFT
Janus monolayer
Thermoelectric performance
Phonon transport properties

ABSTRACT

The exploration of novel, atomically thin, and stable two-dimensional (2D) materials remains an important and active area of study, driving progress in both fundamental science and practical applications within contemporary materials research, particularly in electronic, thermoelectric, and optical domains. Through first-principles density functional theory (DFT) calculations, Three semiconducting Janus monolayers was systematically investigated: SbSI, SbSeI and SbTeI. The comprehensive analysis demonstrates excellent dynamical and energetic stability, indicating the feasibility of mechanical exfoliation for experimental realization. Electronic structure calculations reveal indirect bandgaps of 1.57 (2.12), 1.30 (1.80), and 1.22 (1.64) eV for SbSI, SbSeI, and SbTeI, respectively, using PBE (HSE06) functionals, with the SbSeI monolayer exhibiting an exceptional electron mobility of 213.96 $cm^2V^{-1}s^{-1}$, surpassing that of the well-established MoS_2. Remarkably, at 800 K, the SbSeI monolayer achieves outstanding thermoelectric performance, characterized by a figure of merit (ZT) of 5.39, facilitated by an ultralow lattice thermal conductivity of 0.14 W/mK. Furthermore, upon application of +8% biaxial strain, the SbTeI monolayer displays notable optical properties, including a high reflectivity of 64.00% in the ultraviolet region (~ 250 nm) and an absorption coefficient of 121.98 × 10^4 cm^{-1}. These findings underscore the significant potential of Janus SbXI (X = S, Se, Te) monolayers for next-generation energy conversion applications, offering promising avenues for efficient energy harvesting and thermal management while enabling novel functionalities in nanoscale optical devices.

Introduction

Environmental challenges and energy scarcity have become critical global concerns, prompting the European OECD countries to commit to reducing CO_2 emissions by 80%–95% by 2050 [1,2]. This ambitious target has intensified research efforts in renewable energy technologies to address both environmental protection and human health concerns [3–5]. The scientific community has focused on developing sustainable solutions across multiple domains, including toxic gas detection and elimination [6,7], photovoltaic technology [8,9], optoelectronic devices [10,11], and thermoelectric systems [12,13]. Among these technologies, thermoelectric devices offer unique advantages: they operate noiselessly without moving parts and can directly convert heat into electrical energy through the Seebeck effect (or vice versa via the Peltier effect). This capability enables the development of self-powered smart electronic devices for diverse applications [14,15]. The performance of thermoelectric materials is quantified by a dimensionless figure of merit, ZT:

$$ZT = \frac{S^2\sigma T}{\kappa} \quad (1)$$

where S represents the Seebeck coefficient, σ the electrical conductivity, T the temperature, and κ the total thermal conductivity ($\kappa = \kappa_e + \kappa_l$, comprising electronic κ_e and lattice κ_l contributions) [16,17]. A higher ZT value (particularly above 2) indicates superior performance in power generation and cooling applications [18,19]. In the pursuit of enhanced thermoelectric efficiency, two-dimensional (2D) materials have emerged as promising candidates. These materials demonstrate significant advantages over conventional semiconductors, exhibiting unique structural, electronic, optical, and mechanical properties [14,

* Corresponding authors.
E-mail addresses: gonzalofredy.10@gmail.com (F.M. Gonzalo), emamanif@unjbg.edu.pe (E.M. Flores).

https://doi.org/10.1016/j.rinp.2025.108288
Received 12 December 2024; Received in revised form 17 April 2025; Accepted 1 May 2025
Available online 16 May 2025

15]. Recent studies have shown remarkable progress in this direction. For instance, Z. Lu et al. [20] fabricated flexible thin films of $Sb_{1.5}Bi_{0.5}Te_3$ nanoparticles, achieving a power factor of 183 μW m^{-1} K^{-2}. More recently, theoretical predictions for Janus structures have shown even more promising results: W. Tao et al. [19] predicted a high ZT of 2.54 at elevated temperatures for p-type monolayer PtSeTe, while M. Jakhar et al. [21] demonstrated that Janus β-PdSeTe monolayer could achieve a ZT of 4.09 at 800 K. One effective strategy to improve ZT is through band structure engineering. Y. Pei et al. [22] demonstrated this approach by controlling the doping concentration in $PbTe_{1-x}Se_x$, achieving a ZT of 1.8 at 850 K. Similarly, the Janus LiZnAs monolayer exhibited a remarkably high ZT of 4.16 at 500 K for p-type doping, attributed to its low lattice thermal conductivity of 0.52 W m^{-1} K^{-1} [23]. These studies underscore the importance of minimizing lattice thermal conductivity while maintaining favorable electronic properties to enhance thermoelectric efficiency.

Despite these advancements, the search for novel 2D materials with enhanced thermoelectric properties remains crucial for practical applications. Among potential candidates, Janus monolayers of the SbXI family (X = S, Se, Te) represent an unexplored frontier in thermoelectric research [24]. These materials are particularly promising due to their predicted structural stability and the potential for tuning their electronic and thermal properties through compositional variation and strain engineering. While some studies have investigated similar systems [25], a comprehensive analysis of the strain-dependent of SbXI Janus monolayers is still lacking.

In this work, density functional theory combined with Boltzmann transport theory is employed to systematically investigate the structural, electronic, optical, and thermoelectric properties of SbSI, SbSeI, and SbTeI monolayers. This comprehensive theoretical approach elucidates the potential of these materials for next-generation thermoelectric devices and provides insights into the quantum mechanical principles underlying their properties.

Computational details

First-principles calculations were performed within the framework of density functional theory (DFT) as implemented in the Quantum ESPRESSO package [26]. The electron–ion interactions were described using the projector augmented-wave (PAW) method [27], while the electron exchange–correlation effects were treated with the Perdew–Burke–Ernzerhof (PBE) functional [28]. To account for van der Waals interactions, the DFT-D3 correction scheme proposed by Grimme [29] was employed. The electronic structure was further refined using the hybrid Heyd–Scuseria–Ernzerhof (HSE06) functional [30] to address the well-known bandgap underestimation associated with standard DFT.

Structural optimizations were performed until the Hellmann–Feynman forces on each atom were less than 1×10^{-4} Ry/Bohr, with an energy convergence criterion of 10^{-10} Ry for self-consistent field calculations. The Brillouin zone was sampled using a 10 × 10 × 1 Monkhorst–Pack **k**-point mesh, and the plane-wave basis set was expanded up to a kinetic energy cutoff of 70 Ry. Convergence tests for the energy cutoff and **k**-point sampling are provided in the Supplementary Information (Figs. S1 and S2).

The lattice thermal conductivity was computed by solving the linearized Boltzmann transport equation (LBTE) [31], utilizing both harmonic and anharmonic interatomic force constants (IFCs). Harmonic (second-order) IFCs were calculated using the finite displacement method as implemented in Phonopy [32], employing 7 × 7 × 1 supercells with a 2 × 2 × 1 **k**-point grid. The rotational sum rules were enforced according to Born–Huang constraints [33] using HiPhive [34]. Anharmonic (third-order) IFCs were computed using 4 × 4 × 1 supercells with Phono3py [35], considering interactions within a cutoff radius of <7.06 Å. For accurate phonon transport calculations, a dense 70 × 70 × 1 **q**-point grid was employed.

To account for the two-dimensional nature of the system in thermal conductivity calculations, a thickness correction factor of $L_z = z/h_{eff}$ [36] was applied, where z is the unit cell length in the out-of-plane direction and h_{eff} is the effective monolayer thickness based on the van der Waals radii (I: 1.87 Å, S: 1.66 Å, Se: 1.76 Å, Te: 1.95 Å).

The electronic transport properties, which are crucial for evaluating thermoelectric performance, were assessed using the Boltzmann transport equation as implemented in BoltzTraP2 [37], within the constant relaxation time approximation (CRTA). A dense 100 × 100 × 1 **k**-point mesh was employed for accurate electronic transport calculations. Carrier mobilities were estimated using the deformation potential theory developed by Bardeen and Shockley [38]. Subsequently, all thermoelectric properties were computed in the temperature range of 300–800 K at 100 K intervals.

Results and discussion

Structural properties

The Janus SbXI (X = S, Se, Te) monolayers exhibit a distinctive 1T-phase structure, characteristic of the $P3m1$ space group. This configuration arises from the strategic placement of X atoms (S, Se, or Te) within the SbXI framework, resulting in the Janus arrangement under investigation. Fig. 1 presents the optimized top and side views of these monolayers, illustrating their hexagonal primitive cells composed of Sb, X (S, Se, Te), and I atoms. Notably, these Janus SbXI monolayers demonstrate a propensity for planar configuration, reminiscent of graphene's structural behavior. Our density functional theory (DFT) calculations yield optimized lattice constants ($a = b$) for SbSI, SbSeI, and SbTeI monolayers of 4.08 Å, 4.14 Å, and 4.30 Å, respectively (Table 1). These values align closely with recent computational studies, which report 4.07 Å for SbSI [39], 4.12 Å for SbSeI [40], and 4.32 Å for SbTeI [41,42], underscoring the reliability of our structural optimizations. The charge density distributions, visualized in Fig. 2, reveal robust chemical bonding between Sb, X, and I atoms. This bonding pattern is indicative of significant thermal stability, a crucial factor for potential applications. To further corroborate the stability, the phonon dispersion curves and atom-projected phonon density of states (DOS) were analyzed for all SbXI (X = S, Se, Te) monolayers, as shown in Fig. 3. The absence of imaginary frequencies across the entire Brillouin zone confirms the dynamical stability of these structures and also ensures an accurate description of the lattice thermal conductivity, given its strong sensitivity to the phonon modes [43,44]. Furthermore, the phonon DOS reveals that the low-frequency modes are primarily dominated by the heavier Sb, Te and halogen (I) atoms, while the lighter chalcogen atoms (Se, S, Te) contribute significantly to the higher-frequency vibrational modes. This distribution reflects the mass-dependent vibrational characteristics of each atomic species and further supports the robustness and experimental viability of these monolayers.

To quantitatively assess the thermodynamic stability and formation tendency of these compounds, the cohesive energy (E_{coh}) was calculated, defined as [45]:

$$E_{coh} = \frac{E_{Tot} - n_{Sb}E_{Sb} - n_X E_x - n_I E_I}{n_{Sb} + n_X + n_I} \quad (2)$$

where E_{Tot} represents the total energy of the monolayer, while E_{Sb}, E_X and E_I denote the energies of isolated Sb, X (S, Se, or Te), and I atoms, respectively. The terms n_{Sb}, n_X, and n_I correspond to the number of each atom type in the unit cell. Our calculations reveal cohesive energies of −343.41 meV/atom, −799.32 meV/atom, and −299.88 meV/atom for SbSI, SbSeI, and SbTeI monolayers, respectively (Table 1). These negative values indicate favorable formation energetics, suggesting that these Janus structures are thermodynamically stable and potentially synthesizable.

Interestingly, the cohesive energy trend (SbSeI < SbSI < SbTeI) does not follow the atomic number progression of the X elements. This

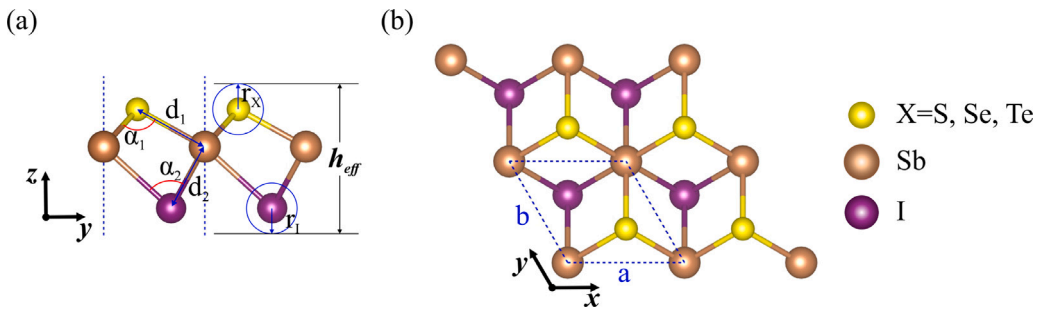

Fig. 1. Optimized structures of Janus SbXI (X = S, Se, Te) monolayers: (a) Side view and (b) top view. Brown spheres represent Sb atoms, yellow spheres denote S, Se, or Te atoms, and purple spheres indicate I atoms. (For interpretation of the references to color in this figure legend, the reader is referred to the web version of this article.)

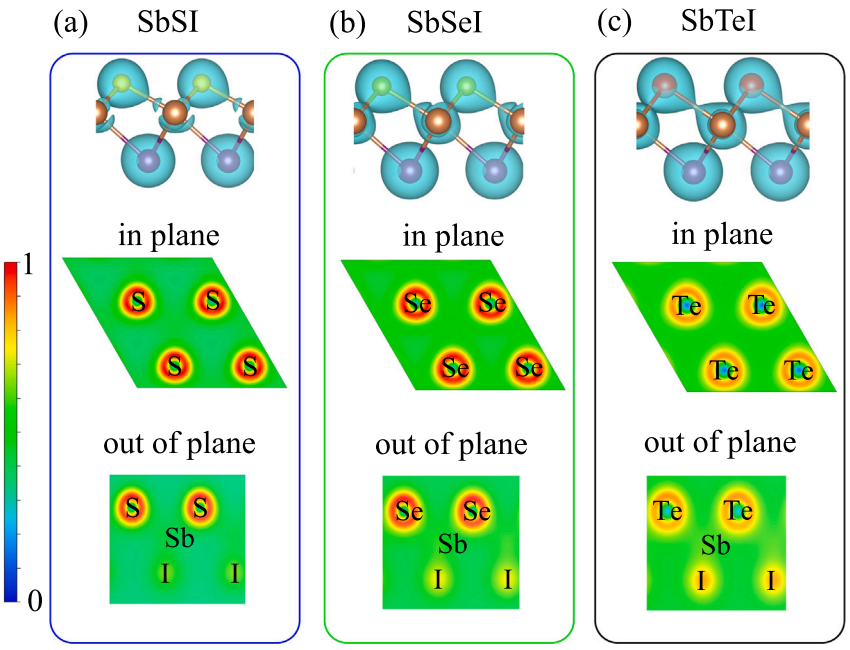

Fig. 2. Partial charge density and Electron Localization Function (ELF) for (a) SbSI, (b) SbSeI, and (c) SbTeI Janus monolayers, shown for in-plane (001) and out-of-plane (100) slices.

Table 1
Structural and electronic properties of Janus SbXI (X = S, Se, Te) monolayers: lattice constants a and b (Å), bond lengths d_1 and d_2 (Å), bond angles α_1 and α_2 (°), effective thickness h_{eff} (Å), cohesive energy E_{coh} (meV/atom), and bandgaps calculated using PBE and HSE06 functionals (eV).

Monolayer	a	d_1	d_2	α_1	α_2	h_{eff}	E_{coh}	E_g^{PBE}	E_g^{HSE06}
SbSI	4.08	4.89	3.19	98.05	79.53	7.00	−343.41	1.57	2.12
SbSeI	4.14	2.82	3.20	94.66	52.32	7.24	−799.32	1.30	1.80
SbTeI	4.30	3.01	3.22	91.50	53.21	7.55	−299.88	1.22	1.64

non-monotonic behavior suggests a complex interplay between atomic size, electronegativity, and bond strength in determining the overall stability of these Janus structures. The significantly lower cohesive energy of SbSeI implies a particularly stable configuration, which may have implications for its potential applications and ease of synthesis.

The structural analysis presented here lays a solid foundation for understanding the fundamental properties of Janus SbXI monolayers. Their stable configurations, coupled with the unique electronic distribution arising from their asymmetric structure, suggest promising potential for tailoring their properties through strain engineering or chemical functionalization. These findings pave the way for further investigations into their electronic, optical, and thermoelectric properties, which will be explored in the following sections.

Electronic properties

The emergence of two-dimensional (2D) Janus materials has opened new avenues for tailoring electronic properties at the atomic scale. Understanding these properties is crucial for advancing applications in nanoelectronics and optoelectronics. Here, a comprehensive analysis of the electronic characteristics of Janus SbXI (X = S, Se, Te) monolayers was presented, which exhibit promising semiconducting behavior. All three monolayers exhibit indirect bandgap semiconducting behavior, with the conduction band minimum (CBM) consistently located at the Γ point and the valence band maximum (VBM) positioned between the K-Γ points. The PBE-calculated bandgaps show a systematic trend: 1.57 eV (SbSI), 1.30 eV (SbSeI), and 1.22 eV (SbTeI), aligning well with previous studies [39,41,46]. To address the known bandgap underestimation of PBE, additional calculations using the HSE06 hybrid functional was performed. As illustrated in Fig. 4, these calculations confirmed the indirect bandgap nature of all three monolayers while yielding more accurate bandgap values: 2.12 eV for SbSI (1.90 eV [47]), 1.80 eV for SbSeI (1.85 eV [48]), and 1.64 eV for SbTeI (1.73 eV [48]).

These values are particularly significant as they determine the minimum photon energy required for electron excitation in potential photocatalytic applications. Orbital-projected band structure analysis provides crucial insights into the electronic character of these materials. Fig. 4(a) shows that in SbSI, the conduction band is primarily

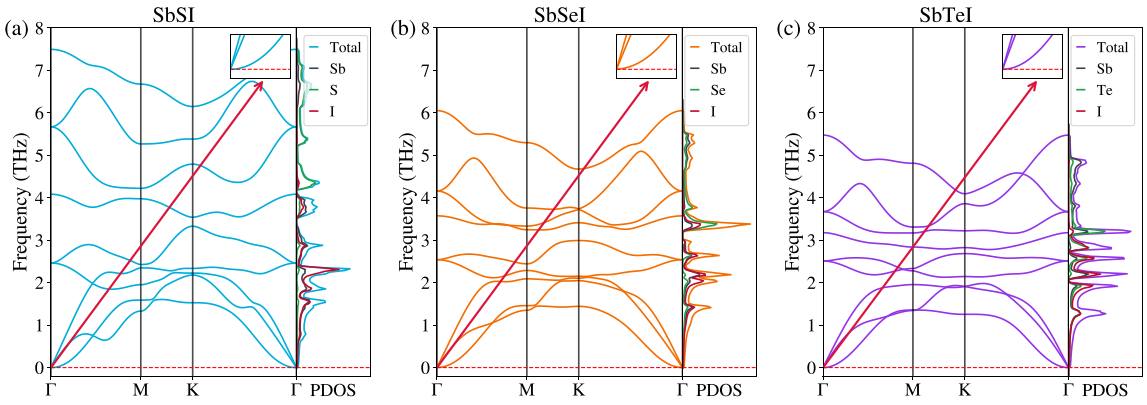

Fig. 3. Phonon dispersion curves and phonon DOS for Janus (a) SbSI, (b) SbSeI, and (c) SbTeI monolayers, demonstrating their dynamical stability.

Table 2
Summarizes our calculated values for effective mass of electrons and holes m^*, carrier mobility μ_{2D} (cm^2/Vs), deformation potential constant E_d (eV), elastic modulus C_{2D} (N/m), and relaxation time τ (fs) along x and y direction at 300 K for Janus SbXI (X = S, Se, Te) monolayers.

Carrier	Monolayer	m_x^*/m_0	m_y^*/m_0	μ_x^{2D}	μ_y^{2D}	E_d^x	E_d^y	C_{2D}^x	C_{2D}^y	τ_x	τ_y
Electron	SbSI	0.36	0.36	69.61	69.60	−8.01	−8.01	27.48	27.48	14.33	14.33
	SbSeI	0.29	0.29	79.69	79.69	−9.43	−9.43	28.52	28.53	13.27	13.27
	SbTeI	0.22	0.22	103.18	102.17	−10.51	−10.56	26.01	26.12	12.94	12.81
Hole	SbSI	0.37	0.37	103.53	103.53	−6.36	−6.36	27.48	27.48	22.01	22.00
	SbSeI	0.31	0.31	213.87	213.96	−7.29	−7.29	28.52	28.53	37.51	37.51
	SbTeI	0.17	0.12	119.60	119.60	−7.23	−7.23	26.01	26.12	20.23	20.23

contributed by Sb, while the valence band exhibits hybridization with contributions from S and I. From Fig. 4(b), in SbSeI, both Sb and Se contribute to the conduction band, while the valence band is dominated by Se. In SbTeI, Te contributes significantly to both the conduction and valence bands, indicating increased chalcogen character as the atomic number increases, as seen in Fig. 4(c). This trend correlates with the observed bandgap reduction across the monolayers.

To assess the potential of these materials for electronic applications, several key parameters was calculated, including effective mass, carrier mobility, and relaxation time. The deformation potential method proposed by Bardeen and Shockley [38] was employed. The effective mass (m^*) is calculated using:

$$m^* = \hbar^2 \left[\frac{\partial^2 E(k)}{\partial k^2} \right]^{-1} . \tag{3}$$

The carrier mobility (μ_{2D}), a crucial parameter for electronic device performance, is given by:

$$\mu_{2D} = \frac{e\hbar^3 \frac{\partial E_s}{\partial \varepsilon_{uni}^2}}{S_0 k_B T m^* \overline{m} E_d^2} , \tag{4}$$

where e is the electron charge, $\hbar$ is the reduced Planck constant, S_0 is the unit cell area, and E_s represents the strain energy difference between the deformed and undeformed unit cells, k_B is the Boltzmann constant, T is the temperature (set to 300 K) and $\overline{m}$ represents the average of m^*. Eq. (4) describe the velocity at which free electrons and holes move within a semiconductor under the influence of an electric field. Another parameter involved in the calculation of τ is the two-dimensional elastic modulus (C_{2D}), which is calculated by fitting the energy–strain curve and parabolic function along the x and y directions for electrons and holes. Also, in Eq. (4), $\overline{m} = \sqrt{m_x m_y}$ represents the geometric average of the effective mass in x and y directions. It can be obtained the deformation potential constant $E_d = \frac{\Delta E_{edge}}{\varepsilon_{uni}}$ for holes and electrons calculating its energy shift (ΔE_{edge}) applying uniaxial strain $\varepsilon_{x/y}$ as can be observed in Fig. S3.

Analysis of the calculated electronic transport parameters reveals several significant trends across the Janus SbXI (X = S, Se, Te) monolayers. Firstly, both electron and hole effective masses exhibit a decreasing trend from SbSI to SbTeI. This reduction in effective mass suggests the potential for higher carrier mobilities in the Te-based structures, which could be advantageous for electronic applications requiring rapid charge transport (see Table 2). Of particular note is the exceptionally high carrier mobility observed in the SbSeI monolayer hole, reaching 213.96 $cm^2\ V^{-1}\ s^{-1}$. It is important to note, however, that in materials where polar optical phonon scattering is not considered due to the use of the deformation potential model, the estimated carrier mobility may be significantly overestimated. This value surpasses the mobility of many well-established two-dimensional semiconductors, including MoS_2 [49], positioning SbSeI as a promising candidate for p-type electronic devices. The high hole mobility, coupled with the material's unique Janus structure, opens up possibilities for novel device architectures and applications in nanoelectronics. Examining the anisotropy of the electronic properties, the most parameters exhibit similar values along the x and y directions. This near-isotropy of in-plane electronic properties is a favorable characteristic for device design and fabrication, as it simplifies the considerations for charge transport in different crystallographic orientations. Interestingly, the deformation potential (E_d) values show an increasing trend from Te to S-based structures, as show in Table 2. This suggests stronger electron–phonon coupling in the heavier chalcogen-based monolayers, which may have significant implications for carrier scattering mechanisms and, consequently, for the temperature-dependent electronic properties of these materials. Further investigation of these electron–phonon interactions could provide valuable insights into the behavior of these materials under various operating conditions. These trends in electronic properties across the SbXI series demonstrate the potential for fine-tuning material characteristics through chalcogen substitution, offering a versatile platform for designing two-dimensional semiconductors with tailored electronic properties for specific applications.

Phonon transport properties and lattice thermal conductivity

The lattice thermal conductivity associated with phonon modes, denoted as $\kappa^{\alpha\beta}$, is calculated using the linearized Boltzmann transport equation (LBTE). This conductivity can be expressed in Cartesian

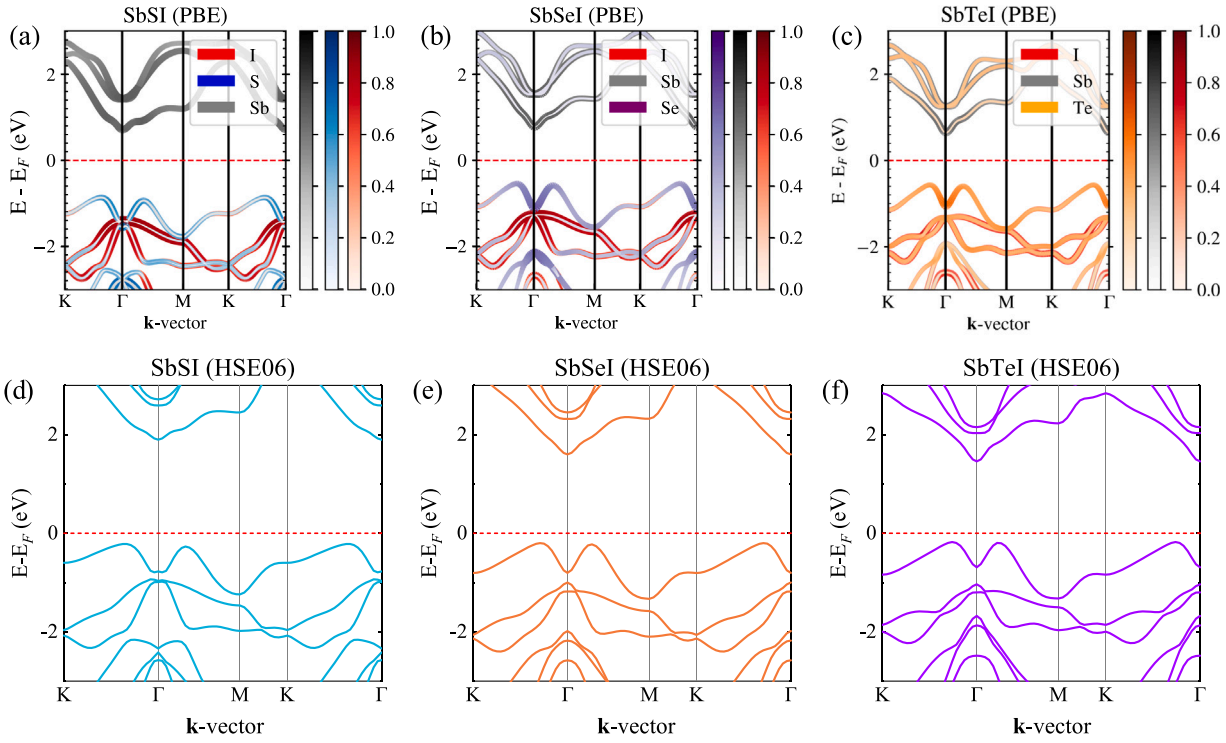

Fig. 4. Atom-projected band structures for Janus (a,d) SbSI, (b,e) SbSeI, and (c,f) SbTeI monolayers calculated using PBE and HSE06 functionals. The Fermi level is set to 0 eV.

components as:

$$\kappa^{\alpha\beta} = \sum_{\lambda} \frac{1}{k_B T^2 V} \times \langle f_0(\omega_{\mathbf{q},\lambda};T)[1+f_0(\omega_{\mathbf{q},\lambda};T)](\hbar\omega_{\mathbf{q},\lambda})^2 v^{\alpha}_{\mathbf{q},\lambda} F^{\beta}_{\mathbf{q},\lambda}\rangle_{\mathbf{q}} \,. \tag{5}$$

where $\mathbf{q}$ represents the wave vector in reciprocal space, and the equilibrium distribution function $f_0(\omega_{\mathbf{q},\lambda};T)$ is evaluated at angular frequency $\omega_{\mathbf{q},\lambda}$ and temperature T. The vector $F_{\mathbf{q},\lambda}$, derived from solving the LBTE, is linked to the phonon lifetime [50]. The notation $\langle\cdots\rangle_{\mathbf{q}}$ indicates averaging over the first Brillouin zone. The group velocity $v_{\mathbf{q},\lambda}$ and phonon lifetime τ_λ are related through:

$$v_{\mathbf{q},\lambda} = \frac{\partial\omega_\lambda}{\partial\mathbf{q}}, \tau_\lambda = \frac{1}{2\Gamma_\lambda(\omega_\lambda)} \,, \tag{6}$$

where $\Gamma_\lambda(\omega_\lambda)$ behaves similarly to Fermi's golden rule. To quantify anharmonicity, the Grüneisen parameter γ was introduced, defined as:

$$\gamma_\lambda(\mathbf{q}) = -\frac{a}{\omega_\lambda}\frac{\partial\lambda}{\partial a} \,, \tag{7}$$

with a being the lattice parameter. A higher average value of $|\gamma|$ corresponds to increased anharmonicity, leading to enhanced phonon–phonon scattering, which inversely affects lattice thermal conductivity κ_l [51].

The lattice thermal conductivity is a crucial parameter for optimizing thermoelectric efficiency in materials [52,53]. As illustrated in Fig. 5(a), the calculated κ_l values for SbSI are 0.30 (0.17) W/m K at 300 (800) K, while for SbSeI, the values are 0.32 (0.14) W/m K, and for SbTeI, 0.36 (0.20) W/m K. Notably, SbSeI exhibits the lowest lattice contribution at 800 K, suggesting a potentially higher figure of merit (ZT). All three materials show isotropic behavior along the x and y axes, however, the calculated value for SbTeI is lower than that reported in [41], where a lattice thermal conductivity of 0.71 W/m K was obtained, where the authors used the product of the unit cell length and the assumed thickness to normalize the results. In contrast, in our study, the lattice thermal conductivity κ_l was normalized using L_z, following a consistent approach for 2D materials [54].

This low lattice thermal conductivity primarily arises from reduced group velocities and limited phonon lifetimes, as shown in Fig. S4 and summarized in Tab. S1. Our analysis indicates that the optical phonon modes significantly contribute to the lattice thermal conductivity, with contributions of 65.58%, 45.22%, and 50.92% for SbSI, SbSeI, and SbTeI, respectively. Conversely, the acoustic ZA modes account for 4.34% (SbTeI), 7.83% (SbSI), and 19.36% (SbSeI) of κ_l. These contributions are depicted in Fig. 5(b), (e), and (h) as functions of frequency.

Although optical phonons are often considered negligible in many materials, certain compounds, such as $BaSnS_2$, demonstrate significant contributions from optical modes, with contributions reaching up to 68% [55]. Our findings suggest a clear indication of anharmonicity in the studied monolayers, particularly noticeable at low frequencies between the acoustic and optical modes, as shown in Fig. 3. The absence of a gap between these modes leads to pronounced anharmonicity, resulting in low group velocities and phonon lifetimes, alongside high Grüneisen parameter values of 1.33, 1.90, and 1.64 for SbSI, SbSeI, and SbTeI, respectively. These values are comparable to or exceed those of well-known thermoelectric materials like $CoSb_3$ (γ = 0.95) [56] and PbTe (γ = 1.4) [57]. To comprehensively assess the factors influencing low lattice thermal conductivity, it is essential to ensure that the rotational invariance conditions are satisfied prior to calculations. This guarantees that the out-of-plane (ZA) mode remains strictly quadratic near the gamma point. The rotational summation technique outlined by Born and Huang [33] should be employed, as neglecting it could lead to significant variations in lattice thermal conductivity results, given the sensitivity of phonon modes to minor changes or imaginary frequencies [43,58].

Fig. 5(c), (f) and (i) illustrates the lattice thermal conductivity, exhibits multiple peaks across the frequency spectrum, reflecting the complex interactions of phonons within the material. Notably, the acoustic modes (ZA, TA, LA) dominate the thermal conductivity at lower frequencies, suggesting efficient heat transport mechanisms facilitated by these modes. As the frequency increases, the contributions from optical modes become apparent, although their influence is secondary to that of the acoustic modes.

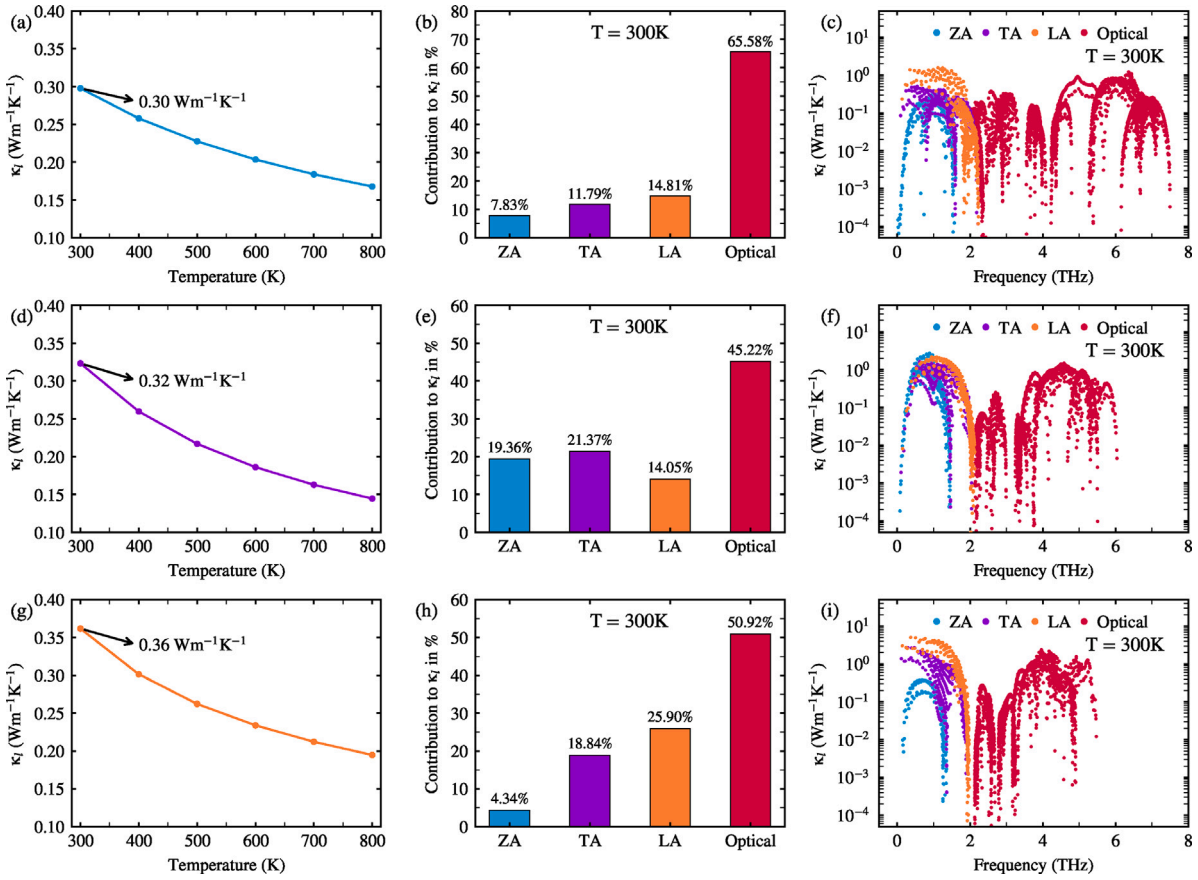

Fig. 5. (a, d, g) Temperature-dependent lattice thermal conductivity, (b, e, h) Contributions of ZA, TA, LA, and optical modes to the lattice thermal conductivity, and (c, f, i) Lattice thermal conductivity as a function of frequency at 300 K. The first, second, and third rows correspond to Janus SbSI, SbSeI, and SbTeI monolayers.

Thermoelectric properties

To assess the efficiency of Janus SbXI (X = S, Se, Te) monolayers, it was calculated the key thermoelectric parameters: the Seebeck coefficient (S), electrical conductivity (σ), electronic thermal conductivity (κ_e), and lattice thermal conductivity (κ_l). These calculations employed the relaxation time (τ) derived from the deformation potential method. The Seebeck coefficient and electrical conductivity exhibit an inverse relationship, both influenced by temperature and chemical potential. As temperature increases, both parameters generally decrease. According to the Wiedemann–Franz law [59], which establishes a proportional relationship between electrical conductivity and electronic thermal conductivity ($\kappa_e = \sigma LT$), higher electrical conductivity corresponds to higher electronic thermal conductivity.

The electronic thermal conductivity (κ_e) is inversely related to the figure of merit (ZT). Consequently, increasing electrical conductivity results in a corresponding increase in electronic thermal conductivity. This relationship underscores the importance of enhancing σ while minimizing thermal conductivity to improve thermoelectric performance.

Fig. 6(a, e, i) presents the calculated Seebeck coefficient around the Fermi level over a chemical potential range of −2 to 2 eV, with temperatures varying from 300 K to 800 K. Negative chemical potentials indicate *p*-type (hole) behavior, while positive values correspond to *n*-type (electron) behavior. The Janus SbSI monolayer demonstrated an *n*-type Seebeck coefficient of 0.85 mV/K at elevated temperatures (800 K), while for the *p*-type, a slightly higher value of 0.92 mV/K was observed. At 300 K, a value of 1.55 mV/K was calculated for both *p*- and *n*-types. These results are shown in Fig. 6(a). The Janus SbSeI monolayer in Fig. 6(e) similarly exhibited a value of 1.55 mV/K for both types at 300 K, but a lower value than SbSI, showing 0.68 mV/K for *n*-type and 0.78 mV/K for *p*-type. Finally, Fig. 6(i) shows the Seebeck coefficient for SbTeI, where at room temperature, S = 1.55 mV/K was calculated for both types, while at 800 K, this value decreased to 0.63 mV/K for *n*-type and 0.73 mV/K for *p*-type. A low Seebeck coefficient could indicate a low ZT due to their direct relationship, as shown in Fig. 6(d, h, l), but ZT also involves parameters like electrical conductivity. Like the Seebeck coefficient, high values of σ are required to increase ZT. The calculated electrical conductivities are shown in Fig. 6(b) for SbSI, (f) for SbSeI, and (j) for SbTeI around the Fermi level. The highest value calculated was 9.61 (10.61) × 10^5 1/Ωm for *n*-type (*p*-type) for SbSI at 300 K. Similarly, SbSeI exhibited a σ of 8.55 (10.90) × 10^5 1/Ωm for *n*-type (*p*-type). The lowest values obtained in this study were for SbTeI, with a σ of 7.86 (8.61) × 10^5 1/Ωm for *n*-type (*p*-type). Conversely, thermal conductivity, requires low thermal conductivity to achieve high thermoelectric efficiency. In Fig. 6, the electronic thermal conductivity as a function of the chemical potential is displayed. For SbSI, a maximum electronic thermal conductivity of 6.96 (7.34) W/m K for *n*-type (*p*-type) was reported at 300 K, while at 800 K, it decreased to 6.19 (6.52) W/m K. For SbSeI, an electronic thermal conductivity of 6.16 (11.88) W/m K was found at 300 K, and at 800 K, values of 5.25 (10.38) W/m K were obtained for *n*-type (*p*-type). Lastly, the Janus SbTeI monolayer exhibited the lowest values among the three, with 5.53 (6.13) W/m K at 300 K and 4.62 (5.97) W/m K for *n*-type (*p*-type). A is minimal variation in the electronic thermal conductivity κ_e occurs as the temperature increases from 300 K to 800 K. This stability suggests that the electronic transport properties of the material remain relatively unaffected over this range, indicating robust performance in varying thermal conditions.

The thermoelectric efficiency is defined by the dimensionless figure of merit (ZT). In this study, a high value of ZT = 0.18 and 1.94 was predicted for SbSI, as shown in Fig. 6(d) for *n*-type and *p*-type,

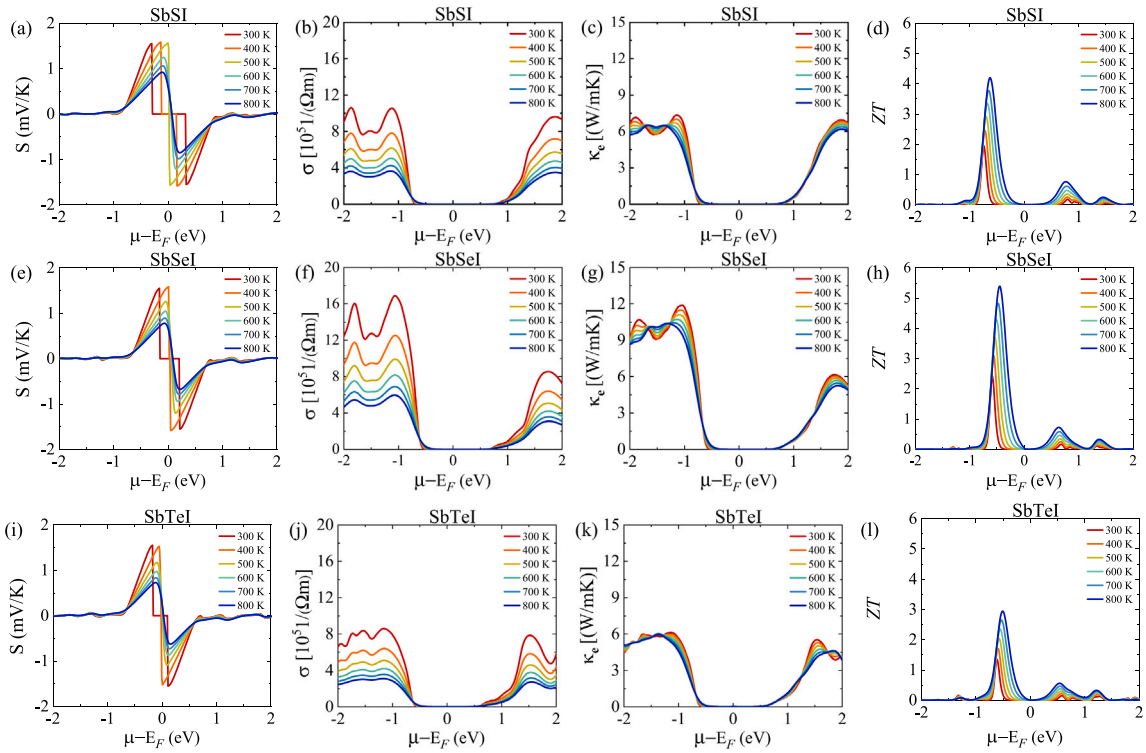

Fig. 6. (a, e, i) Seebeck coefficient, (b, f, j) Electrical conductivity, (c, g, k) Electronic thermal conductivity, and (d, h, l) Figure of merit as a function of chemical potential in a range of 300–800 K at PBE level for Janus SbXI (X = S, Se, Te) monolayers.

Table 3
Thermoelectric properties of *n*-type and *p*-type for Janus SbXI (X = S, Se, Te) monolayers at 300 K and 800 K. Seebeck coefficient S in (mV/K), electrical conductivity σ (10^5 1/Ωm), electronic thermal conductivity κ_e (W/m K), and the thermoelectric figure of merit *ZT*.

Type		300 K				800 K			
	Monolayer	S	σ	κ_e	*ZT*	S	σ	κ_e	*ZT*
n-type	SbSI	1.55	9.61	6.95	0.18	0.85	3.51	6.19	0.76
	SbSeI	1.55	8.55	6.16	0.17	0.68	3.09	5.25	0.73
	SbTeI	1.55	7.86	5.53	0.15	0.63	2.73	4.62	0.56
p-type	SbSI	1.55	10.61	7.34	1.94	0.92	3.65	6.52	4.20
	SbSeI	1.55	16.90	11.88	2.43	0.78	5.96	10.38	5.39
	SbTeI	1.55	8.61	6.13	1.35	0.73	3.10	5.97	2.95

respectively, at room temperature (300 K), while at 800 K, an ultra-high *ZT* of 0.76 (*p*-type: 4.20) was found. The SbSeI monolayer exhibited the highest figure of merit, with 0.73 for *n*-type and 5.39 for *p*-type at 800 K, while at 300 K, values of 0.17 (2.43) were calculated for *n*-type (*p*-type). Lastly, SbTeI showed a maximum *ZT* of 2.95 for *p*-type and 0.56 for *n*-type at 800 K, while at 300 K, its values were 1.35 (0.15) for *n*-type (*p*-type). It was observed that in all cases, *ZT* increased with temperature, as shown in Table 3. Additionally, it was noted that the peak in the *p*-type region was significantly higher than that in the *n*-type region, indicating the predominance of *p*-type charge carriers across the monolayers.

Optical properties

Optical properties of two-dimensional (2D) materials are crucial for their potential applications in optoelectronics. This study employs the Perdew–Burke–Ernzerhof (PBE) method to investigate the optical properties of Janus SbXI (X = S, Se, Te) monolayers, focusing on the optical absorption spectrum with light polarization parallel to the plane. This approach is necessitated by the significant depolarization effects observed in perpendicular polarization for 2D materials. The real and imaginary parts of the dielectric function and the absorption coefficient was evaluated, examining the effects of biaxial strain ranging from −8% to 8% in 4% increments. The negative strain ϵ corresponds to compressive strain, while positive strain indicates tensile strain. The frequency-dependent complex dielectric function $\epsilon(\omega)$ is expressed as:

$$\epsilon(\omega) = \epsilon_1(\omega) + i\epsilon_2(\omega) \tag{8}$$

where the real part ($\epsilon_1(\omega)$) is calculated by the Kramer–Kronig transformation after estimating the imaginary part ($\epsilon_2(\omega)$) based on the crystal wave function $|\mathbf{k}np\rangle$ and its eigenvalue energy $E_{\mathbf{k}n}$ with a crystal momentum $\mathbf{k}$ and spin σ [60].

$$\epsilon_2^{ij}(\omega) = \frac{4\pi^2 e^2}{Vm^2\omega^2} \times \sum_{\mathbf{k}nn'\sigma} \langle \mathbf{k}n\sigma|p_i||kn'\sigma\rangle\langle \mathbf{k}n'\sigma|p_j||kn\sigma\rangle \times f_{\mathbf{k}n}(1 - f_{\mathbf{k}n'})\delta(E_{\mathbf{k}n'} - E_{\mathbf{k}n} - \hbar\omega) \tag{9}$$

where e is the fundamental charge and m its mass, ω is the angular frequency of the incoming photon, V is the volume of the unit cell, $\mathbf{p}$ is the momentum operator ($\mathbf{p} = p_x + p_y + p_z$), and $f_{\mathbf{k}n}$ is the Fermi distribution function. Likewise, the real part can be calculated by

$$\epsilon_1(\omega) = 1 + \frac{2}{\pi} P \int_0^{\infty} \frac{\omega'\epsilon_2(\omega')}{\omega'^2 - \omega^2}. \tag{10}$$

The refractive index, $n^{ij}(\omega)$ is given directly by

$$n^{ij}(\omega) = \left[\frac{\sqrt{\epsilon_1^{ij}(\omega)^2 + \epsilon_2^{ij}(\omega)^2} + \epsilon_1^{ij}(\omega)}{2} \right]^{\frac{1}{2}}, \tag{11}$$

while the refraction index $k^{ij}(\omega)$ can be work out by

$$k^{ij}(\omega) = \left[\frac{\sqrt{\epsilon_1^{ij}(\omega)^2 + \epsilon_2^{ij}(\omega)^2} - \epsilon_1^{ij}(\omega)}{2} \right]^{\frac{1}{2}}, \tag{12}$$

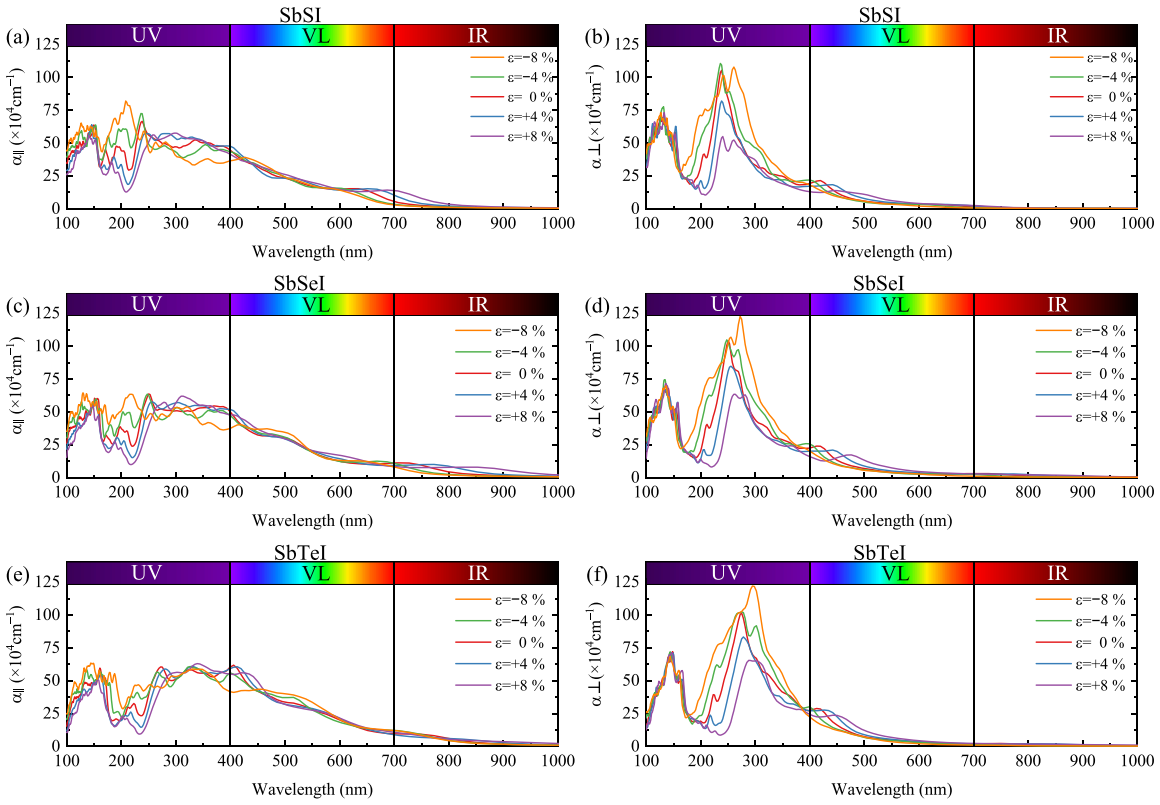

Fig. 7. Absorption coefficient in-plane (a, c, e) and out-of-plane (b, d, f) of Janus SbXI (X = S, Se, Te) monolayer as a function of wavelength under ±8, ±4% biaxial strain.

through Eqs. (11) and (12), the absorption coefficient $\alpha^{ij}(\omega)$ can be obtained using

$$\alpha^{ij}(\omega) = \frac{\sqrt{2}\omega}{c}\left[\sqrt{\epsilon_1^{ij}(\omega)^2 + \epsilon_2^{ij}(\omega)^2} - \epsilon_1^{ij}(\omega)\right]^{\frac{1}{2}} = \frac{4\pi k^{ij}(\omega)}{\lambda}. \tag{13}$$

The reflectivity depends on both $n^{ij}(\omega)$ and $k^{ij}(\omega)$ and is given by

$$R^{ij}(\omega) = \frac{(n^{ij}-1)^2 + k^{ij^2}}{(n^{ij}-1)^2 - k^{ij^2}} \tag{14}$$

The real and imaginary components of the complex dielectric function for SbXI (X = S, Se, Te) are presented in detail in Fig. S5 in the Supplementary Material, where (a) for $\epsilon = 0\%$ shows a peak in the VL range. Similarly, due to the variation of ϵ_1, $\epsilon_2 \parallel$ shows a transition towards the IR region for −4% and −8%, while for +4% and +8%, the maximum value for $\epsilon_1 \parallel$ shifts towards the VL region, with a trend towards the UV. This effect was observed for all three Janus monolayers, as seen in Fig. S5 (a), (e), and (i). In Fig. S5 (c), (g) and (k), the out-of-plane dielectric function is displayed, where it can be observed that anisotropy is exhibited along the polarization directions, $\epsilon_1 \parallel (\omega)$ and $\epsilon_1 \perp (\omega)$.

Furthermore, the absorption coefficient and reflectance properties of the Janus SbXI (X = S, Se, Te) monolayer are shown in Fig. 7 and Fig. S6 obtained thanks to the optical relationship [61] using Eq. (12) and Eq. (11) in Eqs. (13) and (14). In particular, for perpendicular polarization calculated with PBE method, SbSI exhibits a significant absorption peak of 110.48×10^4 cm^{-1} in the UV region ($\lambda = 235.73$ nm), as shown in Fig. 7(b), the highest peak occurs under the compression strain of −4%. SbSeI showed an absorption peak of 122.68×10^4 cm^{-1} with $\lambda = 271.99$ nm located in the UV region. Similarly, SbTeI exhibited the highest peak in the visible region at a wavelength of 294.65 nm, with an absorption coefficient of 121.98×10^4 cm^{-1}, these last two cases occurred for $\epsilon = -8\%$, demonstrating the effectiveness of strain in enhancing the absorption coefficient. In Fig. 7(a, c, e), for parallel polarization or in-plane, it is shown that the absorption coefficient is lower in the UV range; however, there is greater absorption in the visible light (VL) region. On the other hand, both the dielectric function (Fig. S5), where the excitation peaks are located in the visible light (VL) region consistent with [62] and the absorption coefficient (Fig. 7) exhibit peak values within the same wavelength range as those reported in [48].

The initial peaks in the UV region of the optical absorbance, as depicted in Fig. 7, originate from the first interband transitions of electrons from the S/Se/Te-*p* orbitals of the valence bands to the Sb-*p* orbitals of the conduction bands, as shown in Fig. 4. The monolayers studied in this work exhibit a high absorption coefficient for the out-of-plane direction with a predominance in the UV region. These high values of $\alpha_\perp$(nm^{-1}) make these monolayers excellent candidates for solar cells, as there is a direct relationship between the absorption coefficient and the photocurrent. These results are significant in the field of solar cells, as the Janus SbXI (X = S, Se, Te) monolayers absorb energy across UV spectrum, making them highly suitable for optoelectronic and photoelectric applications. The effect of compression and tensile deformation, when compared to the equilibrium state, leads to notable variations in the optical properties. Compressive deformation enhances absorption in the UV region, while tensile deformation induces a decrease in absorption [63–65].

Conclusions

In this work, it was systematically investigated the structural, electronic, and thermoelectric properties of Janus SbXI (X = S, Se, Te) monolayers using first-principles calculations. All three monolayers demonstrated remarkable stability, with SbSeI exhibiting the highest stability (cohesive energy of −799.32 meV/atom). Electronic structure analysis revealed that Sb atoms significantly contribute to the conduction band minimum (CBM) in all cases. Using both PBE and HSE06 functionals, it was found indirect bandgaps of 1.57 (2.12), 1.30 (1.80), and 1.22 (1.64) eV for SbSI, SbSeI, and SbTeI, respectively. The thermoelectric performance analysis showed promising results, particularly

for p-type doping. At 800 K, SbSeI achieved the highest figure of merit (ZT) of 5.39, followed by SbSI (4.20) and SbTeI (2.95). Even at room temperature (300 K), these materials maintained impressive ZT values of 2.43 (SbSeI), 1.94 (SbSI), and 1.35 (SbTeI). These exceptional thermoelectric properties can be attributed to the remarkably low lattice thermal conductivities: 0.30, 0.32, and 0.36 W/m K at 300 K for SbSI, SbSeI, and SbTeI, respectively. Our findings not only demonstrate the potential of Janus monolayers for thermoelectric applications but also highlight their promise for solar energy harvesting, given their strong UV absorption characteristics. This study establishes low lattice thermal conductivity as a key strategy for enhancing thermoelectric efficiency in 2D materials.

CRediT authorship contribution statement

Fredy Mamani Gonzalo: Writing – review & editing, Data curation, Conceptualization. **Victor José Ramirez Rivera:** Methodology, Investigation. **Julio R. Sambrano:** Visualization, Software, Investigation. **Maurício Jeomar Piotrowski:** Validation, Methodology, Investigation. **Efracio Mamani Flores:** Writing – review & editing, Supervision, Investigation.

Funding

This research was made possible by the generous financial support of the Universidad Nacional Jorge Basadre Grohmann, Peru. Funding was provided through the “Fondos del canon, sobrecanon y regalías mineras” program, Peru, as approved by Rectoral Resolution N° 11174-2023-UNJBG.

Declaration of competing interest

The authors declare that they have no known competing financial interests or personal relationships that could have appeared to influence the work reported in this paper.

Acknowledgments

We extend our most sincere gratitude to the Jorge Basadre Grohmann National University, Peru for its continued support of the project “Development of new thermoelectric materials for energy conversion: A theoretical and experimental approach”, approved by Rectoral Resolution N°. 11174-2023-UNJBG.

Supplementary data

Supplementary material related to this article can be found online at https://doi.org/10.1016/j.rinp.2025.108288.

Data availability

No data was used for the research described in the article.

References

[1] Lee ZE, Zhang KM. Scalable identification and control of residential heat pumps: A minimal hardware approach. Appl Energy 2021;286:116544.
[2] Winkler H. Towards a theory of just transition: A neo-Gramscian understanding of how to shift development pathways to zero poverty and zero carbon. Energy Res Soc Sci 2020;70:101789.
[3] Luo H, Guan Q, Lin J, Wang Q, Yang L, Tan Z, Wang N. Air pollution characteristics and human health risks in key cities of northwest China. J Environ Manag 2020;269:110791.
[4] Landrigan PJ, Fuller R, Acosta NJ, Adeyi O, Arnold R, Baldé AB, Bertollini R, Bose-O’Reilly S, Boufford JI, Breysse PN, et al. The lancet commission on pollution and health. Lancet 2018;391(10119):462–512.
[5] Das P, Horton R. Pollution, health, and the planet: time for decisive action. Lancet 2018;391(10119):407–8.
[6] Cui H, Zhang X, Li Y, Chen D, Zhang Y. First-principles insight into Ni-doped InN monolayer as a noxious gases scavenger. Appl Surf Sci 2019;494:859–66.
[7] Wu P, Zhao Z, Huang Z, Huang M. Toxic gas sensing performance of arsenene functionalized by single atoms (Ag, Au): a DFT study. RSC Adv 2024;14(2):1445–58.
[8] kassaye Sibhatu A, Teshome T, Akin-Ojo O, Yimam A, Asres GA. DFT investigation of the electronic and optical properties of hexagonal MX_2/XO (M=W, Mo and X=S, Se) van der Waals heterostructures for photovoltaic solar cell application. RSC Adv 2022;12(47):30838–45.
[9] Jiang Y, Lei S, Jiang Y, Wang M. Highly stable two-dimensional Janus transition metal dichalcogenide-based van der Waals heterostructures for exceptional solar cell performance. Surf Interfaces 2024;52:104830.
[10] Sun Y, Sun N, Zhou W, Ye H. Theoretical prediction of chalcogen-based Janus monolayers for self-powered optoelectronic devices. J Appl Phys 2024;136(10).
[11] Allaoui I, Benyoussef A, El Kenz A, Khuili M. A new two-dimensional MgICl Janus monolayer for optoelectronic applications. Eur Phys J B 2023;96(3):34.
[12] Patel A, Singh D, Sonvane Y, Thakor P, Ahuja R. High thermoelectric performance in two-dimensional Janus monolayer material WS-X (X=Se and Te). ACS Appl Mater Interfaces 2020;12(41):46212–9.
[13] Nautiyal H, Scardi P. First principles study of SnX_2 (X=S, Se) and Janus SnSSe monolayer for thermoelectric applications. Nanotechnology 2022;33(32):325402.
[14] Khan K, Tareen AK, Iqbal M, Shi Z, Zhang H, Guo Z. Novel emerging graphdiyne based two dimensional materials: Synthesis, properties and renewable energy applications. Nano Today 2021;39:101207.
[15] Nithin Chandran B, Thakur A. Two-dimensional materials for green hydrogen production. In: Challenges and opportunities in green hydrogen production. Springer; 2024, p. 379–97.
[16] Shakouri A. Recent developments in semiconductor thermoelectric physics and materials. Annu Rev Mater Res 2011;41(1):399–431.
[17] Yang L, Chen Z-G, Dargusch MS, Zou J. High performance thermoelectric materials: progress and their applications. Adv Energy Mater 2018;8(6):1701797.
[18] Ouyang Y, Xie Y, Zhang Z, Peng Q, Chen Y. Very high thermoelectric figure of merit found in hybrid transition-metal-dichalcogenides. J Appl Phys 2016;120(23).
[19] Tao W-L, Lan J-Q, Hu C-E, Cheng Y, Zhu J, Geng H-Y. Thermoelectric properties of Janus MXY (M=Pd, Pt; X, Y=S, Se, Te) transition-metal dichalcogenide monolayers from first principles. J Appl Phys 2020;127(3).
[20] Lu Z, Layani M, Zhao X, Tan LP, Sun T, Fan S, Yan Q, Magdassi S, Hng HH. Fabrication of flexible thermoelectric thin film devices by inkjet printing. Small 2014;10(17):3551–4.
[21] Jakhar M, Sharma R, Kumar A. Janus β-PdXY (X/Y=S, Se, Te) materials with high anisotropic thermoelectric performance. Nanoscale 2023;15(12):5964–75.
[22] Pei Y, Shi X, LaLonde A, Wang H, Chen L, Snyder GJ. Convergence of electronic bands for high performance bulk thermoelectrics. Nat 2011;473(7345):66–9.
[23] Liu Z, Kuang K, Fang W, Xiao X, Wei H, Chen Y, Li M, He Y. Stability, electronic structures, and thermoelectric properties of 2D Janus LiZnX (X=N, P, As). ACS Appl Energy Mater 2022;5(12):14815–24.
[24] Ozer T, Cabuk S. Ab initio study of the lattice dynamical and thermodynamic properties of SbXI (X=S, Se, Te) compounds. Comput Condens Matter 2018;16:e00320.
[25] Luo W, Ren J, Feng W, Chen X, Yan Y, Zahir N. Engineering nanostructured antimony-based anode materials for sodium ion batteries. Coatings 2021;11(10):1233.
[26] Giannozzi P, Baroni S, Bonini N, Calandra M, Car R, Cavazzoni C, Ceresoli D, Chiarotti GL, Cococcioni M, Dabo I, et al. Quantum espresso: a modular and open-source software project for quantum simulations of materials. J Phys: Condens Matter 2009;21(39):395502.
[27] Blöchl PE. Projector augmented-wave method. Phys Rev B 1994;50(24):17953.
[28] Perdew JP, Burke K, Ernzerhof M. Generalized gradient approximation made simple. Phys Rev Lett 1996;77(18):3865.
[29] Grimme S, Antony J, Ehrlich S, Krieg H. A consistent and accurate ab initio parametrization of density functional dispersion correction (DFT-D) for the 94 elements H-Pu. J Chem Phys 2010;132(15).
[30] Heyd J, Scuseria GE, Ernzerhof M. Hybrid functionals based on a screened Coulomb potential. J Chem Phys 2003;118(18):8207–15.
[31] Chaput L. Direct solution to the linearized phonon Boltzmann equation. Phys Rev Lett 2013;110(26):265506.
[32] Togo A, Tanaka I. First principles phonon calculations in materials science. Scr Mater 2015;108:1–5.
[33] Born M, Huang K. Dynamical theory of crystal lattices. Oxford University Press; 1996.
[34] Eriksson F, Fransson E, Erhart P. The Hiphive package for the extraction of high-order force constants by machine learning. Adv Theory Simul 2019;2(5):1800184.
[35] Togo A, Chaput L, Tadano T, Tanaka I. Implementation strategies in phonopy and phono3py. J Phys: Condens Matter 2023;35(35):353001.
[36] Zhu X-L, Liu P-F, Zhang J, Zhang P, Zhou W-X, Xie G, Wang B-T. Monolayer SnP3: an excellent p-type thermoelectric material. Nanoscale 2019;11:19923–32.
[37] Madsen GK, Carrete J, Verstraete MJ. BoltzTraP2, a program for interpolating band structures and calculating semi-classical transport coefficients. Comput Phys Comm 2018;231:140–5.

[38] Bardeen J, Shockley W. Deformation potentials and mobilities in non-polar crystals. Phys Rev 1950;80(1):72.
[39] Liu H-y, Yang H, Zheng Y. Two-dimensional Janus SbTeBr/SbSI heterostructures as multifunctional optoelectronic systems with efficient carrier separation. Phys Chem Chem Phys 2024;26(7):6228–34.
[40] Chauhan P, Singh J, Kumar A. Two-dimensional Janus antimony chalcohalides for efficient energy conversion applications. J Mater Chem A 2024.
[41] Guo S-D, Zhang A-X, Li H-C. Potential 2D thermoelectric material ATeI (A=Sb and Bi) monolayers from a first-principles study. Nanotechnology 2017;28(44):445702.
[42] Zhuang HL, Cooper VR, Xu H, Ganesh P, Hennig RG, Kent PRC. Rashba effect in single-layer antimony telluroiodide SbTeI. Phys Rev B 2015;92:115302.
[43] Carrete J, Li W, Lindsay L, Broido DA, Gallego LJ, Mingo N. Physically founded phonon dispersions of few-layer materials and the case of borophene. Mater Res Lett 2016;4(4):204–11.
[44] Taheri A, Pisana S, Singh CV. Importance of quadratic dispersion in acoustic flexural phonons for thermal transport of two-dimensional materials. Phys Rev B 2021;103:235426.
[45] Zheng D, Peng W, Wu R, Quan S, Qian L, Cui H. Sensing property of Pt-doped Janus SnSSe monolayer upon thermal runaway gases in the lithium-ion battery with effects of biaxial strains and electric fields. J Environ Chem Eng 2023;11(3):109711.
[46] Li T, Xu Y, Li M, Zhou Q, Wu C, Wang Z, Ju W. A study of the Rashba effect in two-dimensional ternary compounds ABC monolayers (A=Sb, Bi; B=Se, Te; C=Br; I). Phys Chem Chem Phys 2023;25(4):3182–9.
[47] Liu H-y, Yang H, Zheng Y. Two-dimensional Janus SbTeBr/SbSI heterostructures as multifunctional optoelectronic systems with efficient carrier separation. Phys Chem Chem Phys 2024;26:6228–34.
[48] Bafekry A, Faraji M, Fadlallah MM, Hoat DM, Jappor HR, Sarsari IA, Gherghere-hchi M, Feghhi SAH. Electronic, optical and thermoelectric properties of a novel two-dimensional SbXY (X=Se, Te; Y=Br, I) family: ab initio perspective. Phys Chem Chem Phys 2021;23:25866–76.
[49] Zhang Y, Zhao HL, Huang S, Hossain MA, van der Zande AM. Enhancing carrier mobility in monolayer MoS_2 transistors with process-induced strain. ACS Nano 2024;18(19):12377–85.
[50] Chaput L, Togo A, Tanaka I, Hug G. Phonon-phonon interactions in transition metals. Phys Rev B—Condens Matter Mater Phys 2011;84(9):094302.
[51] Lee CH, Gan CK. Anharmonic interatomic force constants and thermal conductivity from Grüneisen parameters: An application to graphene. Phys Rev B 2017;96(3):035105.
[52] Hu R, Zhou Z, Sheng C, Han S, Yuan H, Liu H. Ultralow lattice thermal conductivity and high thermoelectric performance of the WS_2/WTe_2 van der Waals superlattice. Phys Lett A 2022;430:127986.
[53] Min R, Wang Y, Jiang X, Chen R, Li M, Kang H, Yang X, Chen Z, Guo E, Wang T. ZrNiSn-based compounds with high thermoelectric performance and ultralow lattice thermal conductivity via introduction of multiscale scattering centers. J Mater 2024;10(1):200–9.
[54] Bai S, Tang S, Wu M, Luo D, Zhang J, Wan D, Li X. Chromium ditelluride monolayer: A novel promising 2H phase thermoelectric material with direct bandgap and ultralow lattice thermal conductivity. J Alloys Compd 2023;930:167485.
[55] Li Z, Xie H, Hao S, Xia Y, Su X, Kanatzidis MG, Wolverton C, Tang X. Optical phonon dominated heat transport: A first-principles thermal conductivity study of $BaSnS_2$. Phys Rev B 2021;104(24):245209.
[56] Caillat T, Borshchevsky A, Fleurial J-P. Properties of single crystalline semiconducting $CoSb_3$. J Appl Phys 1996;80(8):4442–9.
[57] Morelli D, Jovovic V, Heremans J. Intrinsically minimal thermal conductivity in cubic I-V-VI_2 semiconductors. Phys Rev Lett 2008;101(3):035901.
[58] Taheri A, Pisana S, Singh CV. Importance of quadratic dispersion in acoustic flexural phonons for thermal transport of two-dimensional materials. Phys Rev B 2021;103(23):235426.
[59] Chester G, Thellung A. The law of Wiedemann and Franz. Proc Phys Soc 1961;77(5):1005.
[60] Lucarini V, Saarinen JJ, Peiponen K-E, Vartiainen EM. Kramers-Kronig relations in optical materials research, vol. 110, Springer Science & Business Media; 2005.
[61] Liu W-K, Kong S-S, Yu X-X, Li Y-L, Yang L-Z, Ma Y, Fang X-Y. Interlayer coupling, electronic and optical properties of few-layer silicon carbide nanosheets. Mater Today Commun 2023;34:105030.
[62] Xu H-Q, Xiao G, Xiao W-Z, Wang L-L. Piezoelectricity and optical properties of janus MXY (M=Sb, As; X= Te, Se; Y=Br, I) monolayers. Micro Nanostructures 2022;170:207396.
[63] Xiong M, Chen Z-Y, Hu C-E, Cheng Y, Geng H-Y. First-principles study of strain effect on elastic and optical properties and lattice thermal conductivity of Janus ZrBrCl monolayer. Mater Today Commun 2021;26:101995.
[64] Labani BK, Diery W. First-principles study on electronic structure and optical properties of monolayer Janus PtSTe under external electric field and strain. Eur Phys J Plus 2021;136(12):1–13.
[65] Liu H, Yang L, Zhao Y, Sun S, Wei X. Exploring optoelectronic and thermal characteristics of Janus MoSeTe and WSeTe monolayers under mechanical strain. Mater Today Commun 2024;40:109570.